Check for updates

Controlling Grain Boundary Segregation to Tune the Conductivity of Ceramic Proton Conductors

Moritz Kindelmann, Ivan Povstugar, Severin Kuffer, Dylan Jennings, Julian N. Ebert, Moritz L. Weber, M. Pascal Zahler, Sonia Escolastico, Laura Almar, Jose M. Serra, Payam Kaghazchi, Martin Bram, Wolfgang Rheinheimer, Joachim Mayer, and Olivier Guillon**

Acceptor-doped barium zirconates are of major interest as proton-conducting ceramics for electrochemical applications at intermediate operating temperatures. However, the proton transport through polycrystalline microstructures is hindered by the presence of a positive space charge potential at grain boundaries. During high-temperature sintering, the positive charge acts as a driving force for acceptor dopant segregation to the grain boundary. Acceptor segregation to grain boundaries has been observed in sintered ceramics, but the fundamental relationship between the segregation kinetics and the protonic conductivity is poorly understood. Here, a comprehensive study of the influence of acceptor dopant segregation on the electrochemical properties of grain boundaries in barium zirconate ceramics is presented. An out-of-equilibrium model material that displays no detectable Y segregation at its grain boundaries is explicitly designed. This model material serves as a starting point to measure the kinetics of segregation and the induced changes in grain boundary conductivity upon varying thermal histories. Furthermore, the electrochemical results from impedance spectroscopy to atomic resolution transmission electron microscopy, atom probe tomography, and DFT simulations are correlated. It is discovered that acceptor dopant segregation drastically increases the proton conductivity in both the model system and several other application-relevant compositions.

1. Introduction

Solute segregation to grain boundaries greatly impacts the bulk properties of polycrystalline solids. This includes structural, chemical and functional properties, in metallic and ceramic materials.[1–4] Segregation phenomena are especially important for ceramic ionic and mixed electronic-ionic conductors, where grain boundaries can drastically decrease the ionic transport.[5–7] Ion-conducting ceramics are highly relevant for a wide variety of energy applications ranging from solid state batteries[8,9] to solid oxide fuel and electrolyzer cells[10–14] and membrane reactors,[15–19] and are pivotal for future fossil-free energy systems. Recently, electrochemical devices based on proton-conducting ceramics have shown immense potential due to their reversible and robust performance in different operating modes.[20,21] Enabled by a dissociative hydration of water into oxygen vacancies

---

M. Kindelmann, I. Povstugar, D. Jennings, J. Mayer
Ernst Ruska-Centre for Microscopy and Spectroscopy with Electrons (ER-C)
Forschungszentrum Jülich GmbH
52425 Jülich, Germany
E-mail: m.kindelmann@fz-juelich.de

M. Kindelmann, S. Kuffer, D. Jennings, P. Kaghazchi, M. Bram, O. Guillon
Institute of Energy Materials and Devices
Materials Synthesis and Processing (IMD-2)
Forschungszentrum Jülich GmbH
52425 Jülich, Germany
E-mail: o.guillon@fz-juelich.de

The ORCID identification number(s) for the author(s) of this article can be found under https://doi.org/10.1002/aenm.202404410

© 2024 The Author(s). Advanced Energy Materials published by Wiley-VCH GmbH. This is an open access article under the terms of the Creative Commons Attribution License, which permits use, distribution and reproduction in any medium, provided the original work is properly cited.

DOI: 10.1002/aenm.202404410

D. Jennings, J. N. Ebert, M. P. Zahler, W. Rheinheimer
Institute for Manufacturing Technologies of Ceramic Components and Composites (IFKB)
University of Stuttgart
70569 Stuttgart, Germany

M. L. Weber
Peter Gruenberg Institute for Electronic Materials (PGI-7)
Forschungszentrum Jülich GmbH
52425 Jülich, Germany

S. Escolastico, L. Almar, J. M. Serra
Instituto de Tecnología Química
Universitat Politècnica de València – Consejo Superior de Investigaciones Científicas
Av. Los Naranjos, s/n, Valencia 46022, Spain

P. Kaghazchi
MESA+ Institute for Nanotechnology
University of Twente
P. O. Box 217, Enschede 7500AE, The Netherlands

(Equation 1), the transport of protons is made possible through a combination of reorientation and hopping, generally known as the Grotthuss mechanism.[22]

$$H_2O + V_O^{\cdot\cdot} + O_O^x \rightarrow 2OH_O^{\cdot} \quad (1)$$

Most high-performance proton conducting oxides are based on a solid solution of the perovskites $BaZrO_3$ and $BaCeO_3$ using Y^{3+}, Yb^{3+} or other trivalent dopants as acceptors.[10,22–24] This material system allows the adjustment of the perovskite's stability and conduction properties to meet the operational requirements of specific applications like stability against steam and CO_2 at elevated temperatures.

Barium zirconate-based proton conductors suffer from low grain boundary conductivities due to their positively charged interfaces, caused by oxygen vacancy segregation.[25–28] The accumulation of vacancies leads to the formation of a negatively charged space charge layer (SCL) adjacent to the interface, induced by the redistribution of point defects, hindering the transport of protons.[26,29–31] During high-temperature thermal treatment, the positive core charge at grain boundaries acts as a driving force for the segregation of acceptor dopants to the interface, leading to their enrichment in the grain boundary core and/or the SCL.[29,32,33] The segregation of negatively charged point defects can partially compensate for the positive core charge, leading to an increase in grain boundary conductivity, for example, observed after high temperature thermal annealing of Y and Sc doped $BaZrO_3$.[29,32,34] However, the kinetics of segregation have not been explored due to the lack of a nonequilibrated model system and most reports study segregation only phenomenologically using transmission electron microscopy (TEM)[32,34–37] or atom probe tomography (APT).[33,38,39]

Until now, a fundamental relationship between the kinetics of acceptor dopant segregation and the resulting grain boundary conductivity is lacking. As the formation of acceptor dopant segregation is happening at elevated temperatures, where cationic diffusion is sufficiently high, all conventionally processed samples exhibit a grain boundary defect chemistry that is dependent on their specific thermal history (processing temperature, dwell time, and cooling rate). The measured interfacial chemistry at room temperature is therefore dominated by two restricted equilibria:[40,41] 1) the acceptor dopant concentration is "frozen in" below a critical temperature, where cationic diffusion is extremely slow. 2) below that temperature oxygen vacancies ($V_O^{\cdot\cdot}$) are still mobile, until the interface reaches a third temperature regime where all defects are immobile. So far, the unavoidable equilibration of the grain boundary defect chemistry during high temperature treatment has prevented a systematic investigation of the acceptor segregation kinetics and how this affects the transport properties of ion-conducting ceramics.

Here, we present a comprehensive study on the kinetics of acceptor dopant segregation and its impact on the electrochemical performance of $BaZrO_3$-based proton conductors. Building on the recently discovered, slow cation defect redistribution at grain boundaries in undoped $SrTiO_3$ during low temperature, high-pressure spark plasma sintering,[42] we developed a processing scheme that completely suppresses yttrium acceptor dopant segregation, and therefore allows us to investigate the extent and the kinetics that acceptor segregation poses on the grain boundary conductivity in $BaZrO_3$ based proton conductors. Targeted thermal treatments are used to systematically change the grain boundary properties through controlled acceptor segregation. We correlated the bulk electrochemical properties with the chemical composition and bonding environment at the grain boundary using atomically resolved characterization techniques to reveal that high proton conductivities are enabled by the atomically sharp segregation of yttrium acceptor dopants to the first atomic plane at the grain boundary. The continuous segregation of yttrium to the grain boundaries leads to decreased space charge potentials, enabling high protonic conductivities. Even though this study focuses on the characterization of the protonic ceramic $BaZr_{0.7}Ce_{0.2}Y_{0.1}O_{3\text{-}\delta}$, the phenomenon of segregation-controlled conductivity is demonstrated to be transferable to all highly relevant $BaZrO_3$ based compositions (including $BaZr_{0.8}Y_{0.2}O_{3\text{-}\delta}$ (BZY20), $BaZr_{0.5}Ce_{0.3}Y_{0.2}O_{3\text{-}\delta}$ (BZCY532) and $BaZr_{0.4}Ce_{0.4}Y_{0.1}Yb_{0.1}O_{3\text{-}\delta}$ (BZCYYb441)). Our results clearly illustrate the importance of high-temperature treatments beyond 1300 °C in equilibrating the defect chemistry at grain boundaries in proton-conducting ceramics, which is crucial to facilitate high proton conductivities. Additionally, the presented findings are highly relevant for other oxide-based ionic conductors and electroceramics, where understanding grain boundary segregation might open new possibilities for the design and improvement of material properties.

2. Results and Discussion

2.1. Controlling Conductivity Through Targeted Interfacial Equilibration

Figure 1 compares the conductivity of $BaZr_{0.7}Ce_{0.2}Y_{0.1}O_{3\text{-}\delta}$ (BZCY) ceramics with different thermal histories. To study the impact of various equilibration temperatures, we designed a starting material that has not been equilibrated at high sintering temperatures such as conventionally processed BZCY. Therefore, pure BZCY powders were sintered to high relative densities using field assisted sintering/spark plasma sintering (FAST/SPS). This approach allows the use of high heating and cooling rates (± 150 °C min^{-1}) and a very short dwell time (5 min) at comparably low temperatures (1450 °C).[42,43] This processing procedure yields ultrafine, dense samples (Figure 1b, top, grain size: 350 ± 175 nm), which have a nonequilibrated grain boundary defect chemistry (as shown later), making them an optimal starting point to investigate the relationship between thermal history, acceptor dopant segregation, and grain boundary conductivity. A variation of thermal treatments was applied to systematically change the grain boundary defect chemistry between 1000 and 1600 °C (the schematic in Figure 1a displays the two-step annealing process). Electrochemical impedance spectroscopy (EIS)

J. Mayer
Central Facility for Electron Microscopy (GFE)
RWTH Aachen University
52074 Aachen, Germany

O. Guillon
Jülich Aachen Research Alliance
JARA-Energy
52425 Jülich, Germany

© 2024 The Author(s). Advanced Energy Materials published by Wiley-VCH GmbH

16146840, 2025, 9, Downloaded from https://advanced.onlinelibrary.wiley.com/doi/10.1002/aenm.202404410 by Forschungszentrum Jülich GmbH Research Center, Wiley Online Library on [07/03/2025]. See the Terms and Conditions (https://onlinelibrary.wiley.com/terms-and-conditions) on Wiley Online Library for rules of use; OA articles are governed by the applicable Creative Commons License

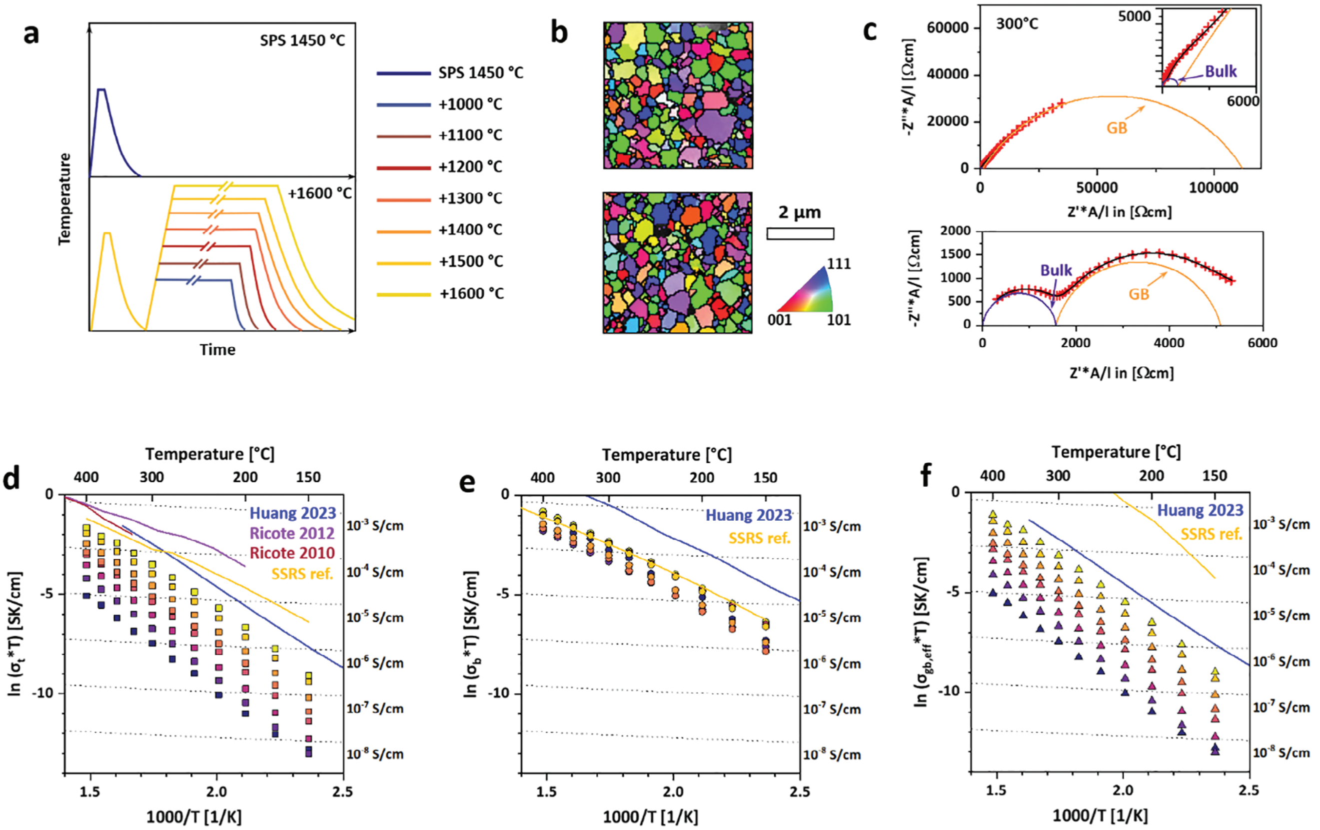

Figure 1. Influence of the thermal history on the grain boundary conductivity of $BaZr_{0.7}Ce_{0.2}Y_{0.1}O_{3-\delta}$. a) Schematic representation of the thermal history for the different BZCY samples shown here. (cooling rates and dwell time are −150 K min^{-1} to 1450 °C and 5 min for the SPS cycle and −5 K min^{-1} and 5 h for the furnace runs). b) EBSD orientation mappings showing no changes in the microstructure of the SPS sample (top) and the +1600 °C sample (bottom). The scale bar is 2 µm. c) Nyquist plots from electrochemical impedance spectroscopy at 300 °C in wet Ar/H_2 of the SPS (top) and +1600 °C sample (bottom). The impedance data for all samples were fitted using two R||CPE circuits to separate the bulk from the grain boundary response and derive the total d), bulk e), and effective grain boundary f). All conductivity plots also include literature values from BZCY ceramics of the same composition[37,44,45] and a reference sample produced by solid state reactive sintering (SSRS with 0.5 wt% NiO) denoted as solid lines.

was used to measure the conductivity at temperatures between 600 and 150 °C in wet Ar/H_2. As a separation of the bulk and grain boundary semicircle above 400 °C is not possible, values between 400 and 600 °C are not displayed here.[46] Therefore, bulk and grain boundary contributions can be compared for the full temperature range. Figure 1c shows two Nyquist plots obtained from EIS measurements at 300 °C in wet Ar/H_2 to highlight the direct changes induced by a thermal treatment at 1600 °C in air. The total impedance is strongly decreased, driven by a massive reduction of the grain boundary contribution. At the same time, the bulk impedance stays in the same order of magnitude. The complete impedance data set, which displays the total, bulk and effective grain boundary conductivities, respectively, is summarized in Figure 1d–f. The total conductivity continuously increases, depending on the extent of the thermal treatment (Figure 1d), and reaches values comparable to samples in literature with the same composition after conventional processing.[37,44,45] Furthermore, we compared our model system to samples processed by the industrially applied solid state reactive sintering method (SSRS) and could also find comparable conductivities. The continuous increase in total conductivity is controlled by the grain boundary conductivity, which shows a comparable behavior (Figure 1f), while the bulk conductivity remains relatively constant (Figure 1e). This effect is independent from the microstructure, as $BaZrO_3$ based materials show a sluggish grain growth behavior, when no sintering aids are added.[47] Microstructure imaging and quantitative analysis (Figure 1b) show that the average grain size after the highest thermal treatment (+1600 °C) is still at 320 ± 172 nm, confirming that no measurable grain growth could be observed. This proves that changes in grain boundary composition and interfacial defect chemistry are most possibly responsible for the strong increase in protonic conductivity after equilibration of the samples at high temperatures, while a relative change in the interfacial area between grain boundaries can be excluded as the origin of the observed effect.

If the segregation of acceptor dopants is the major factor driving the increase in grain boundary conductivity through charge compensation, this should also reduce the space charge potential ϕ_0, which can be derived from EIS data using Equation (2).[48,49]

$$\frac{\omega_{Bulk}}{\omega_{GB}} = \frac{e^{z_j F \phi_0 / RT}}{2\, z_j F \phi_0 / RT} \tag{2}$$

© 2024 The Author(s). Advanced Energy Materials published by Wiley-VCH GmbH

16146840, 2025, 9, Downloaded from https://advanced.onlinelibrary.wiley.com/doi/10.1002/aenm.202404410 by Forschungszentrum Jülich GmbH Research Center, Wiley Online Library on [07/03/2025]. See the Terms and Conditions (https://onlinelibrary.wiley.com/terms-and-conditions) on Wiley Online Library for rules of use; OA articles are governed by the applicable Creative Commons License

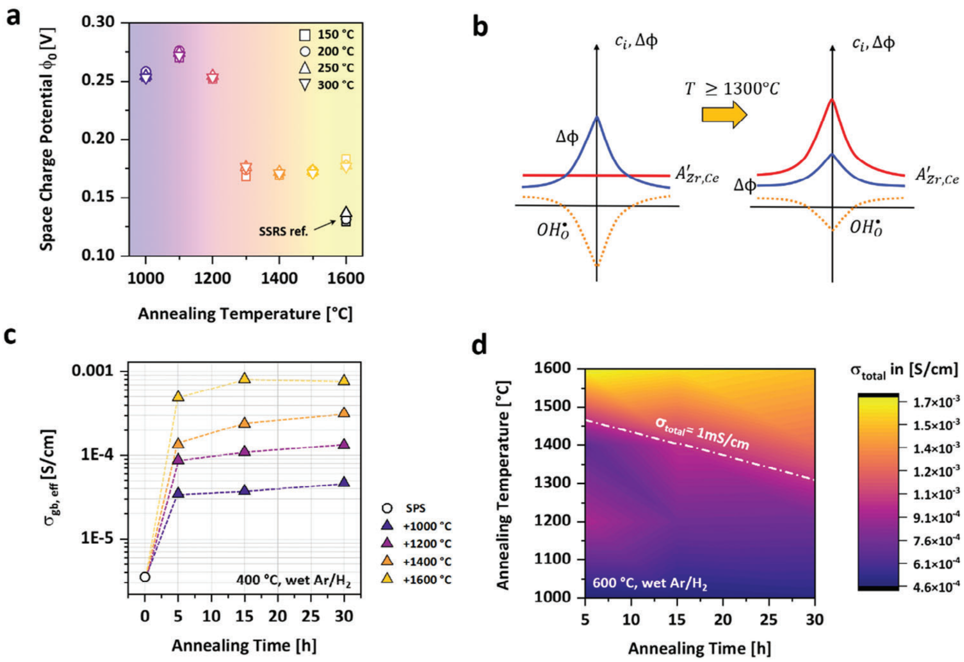

Figure 2. Impact of segregation kinetics on space charge potential and protonic conductivity. a) Space charge potential after varied thermal histories calculated from EIS data using Equation (2). b) Schematic representation of the charge compensation mechanism induced by acceptor segregation during thermal annealing. c) The effective grain boundary conductivity at 400 °C in wet Ar/H$_2$ derived from EIS measurements after different annealing treatments between 1000 and 1600 °C for 5–30 h. d) Processing map showing the total conductivity at 600 °C in Ar/H$_2$ after different equilibration treatments. The dashed line represents a conductivity of 1 mS cm^{-1}.

In Equation (2), R is the Boltzmann constant, F the Faraday constant, Φ_0 the space charge potential, z_j the valency of the mobile charge carrier ($z_j = 1$ for Protons), e the elementary charge, T the temperature in K during EIS and, ω_{Bulk} and ω_{GB} are the relaxation frequencies of the bulk's and GBs' impedance signal. More details about Equation (2) can be found in the methods section. **Figure** 2a displays the space charge potential ϕ_0 for samples after thermal treatments at temperatures between 1000 and 1600 °C. The potential in samples annealed at lower temperatures is the highest, with values ≈0.25–0.27 V. Nevertheless, it is still significantly lower than reported for $BaZrO_3$ based proton conductors (0.5–0.6 V at 250 °C),[36,50] possibly due to high oxygen partial pressure (wet oxidizing atmosphere) used in the referenced studies. Thermal annealing at temperatures above 1300 °C leads to a further significant decrease of the space charge potential down to values of 0.17 V. However, these values lie still above the space charge potential derived from reference samples processed by SSRS, most likely due to additional charge compensation mechanisms induced by the segregation of Ni to the grain boundary (also leading to a high effective GB conductivity observed in Figure 1f).[38,39] Since microstructural changes were not observed in our model samples, the compensation of the positive core charge at the grain boundary through acceptor dopant segregation is possibly the dominant mechanism enabling high grain boundary conductivity. The schematic in Figure 2b explains the basic principle of this mechanism, in which the potential at an interface is significantly higher due to a homogeneous distribution of acceptor dopants across the interface. The thermally activated segregation of negatively charged Y'_{Zr} cations to the interface (driven by the core charge), then compensates for parts of the positive core charge, leading to a reduction of the space charge potential.

To further understand the kinetics of segregation, more extended annealing experiments were conducted at 1000, 1200, 1400, and 1600 °C in a range between 5 and 30 h in air and investigated by EIS. Figure 2c shows the changes in the grain boundary conductivity after these treatments, starting from the nonequilibrated samples state (black circle). Large increases in conductivity can be observed after short annealing times. However, due to insufficient cation diffusion kinetics at temperatures below 1400 °C, a full equilibration could not be achieved for these samples. Since the positive core charge acts as the major driving force for yttrium segregation to the grain boundary, the process decelerates until a balance is reached between further segregation and the interfacial space charge potential.

Even though separation of bulk and grain boundary conductivities is not possible at temperatures above 600 °C, the systematic annealing treatments done here allow us to map out the interfacial equilibration times and temperatures, which are needed to surpass a minimum total conductivity of 1 mS cm^{-1} in wet Ar/H$_2$ (Figure 2d). For the BZCY composition investigated here, temperatures above 1300 °C (and sufficiently long dwell times) enable the progressive grain boundary equilibration and thus, reaching the total conductivity magnitude needed for practical application.

© 2024 The Author(s). Advanced Energy Materials published by Wiley-VCH GmbH

16146840, 2025, 9, Downloaded from https://advanced.onlinelibrary.wiley.com/doi/10.1002/aenm.202404410 by Forschungszentrum Jülich GmbH Research Center, Wiley Online Library on [07/03/2025]. See the Terms and Conditions (https://onlinelibrary.wiley.com/terms-and-conditions) on Wiley Online Library for rules of use; OA articles are governed by the applicable Creative Commons License

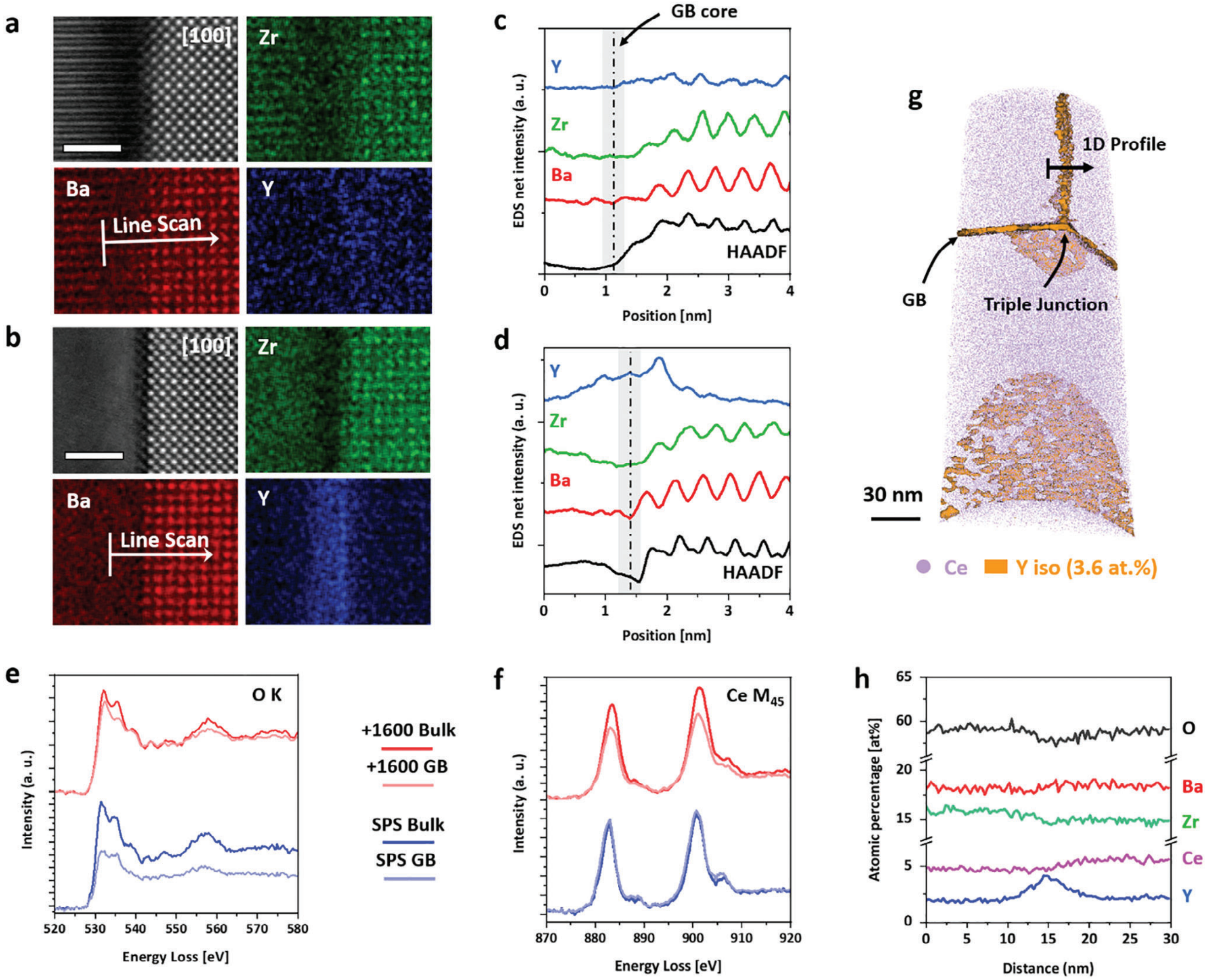

Figure 3. Segregation behavior at BZCY grain boundaries before and after high temperature equilibration. a,b) High resolution STEM images and EDS mappings of general grain boundaries in SPS (a) and +1600 (b) showing the absence before, and the atomically sharp yttrium segregation after thermal annealing. The scale bar is 2 nm. c,d) Integrated line scans (highlighted in the corresponding Ba mapping) reveal the chemical composition at the interface of SPS (c) and +1600 BZCY (d) (dashed lines correspond to the grain boundary core). e,f) EELS spectra of the O K-edge (e) and the Ce M4,5-edge (f) derived from the bulk and the grain boundary core. g) APT elemental map of the +1600 BZCY sample showing Ce atoms and an Y isoconcentration surface (3.6 at%) decorating grain boundaries. The data set contains five grain boundaries and a triple junction. h) a concentration profile of the major elements across the grain boundary indicated in (g).

2.2. Observing Acceptor Segregation at the Atomic Scale

To understand the atomistic reasons for the continuous conductivity increase after thermal treatments at varied temperatures, we investigated grain boundaries in nonequilibrated (SPS) and thermally treated (SPS +1600 °C) samples using high resolution scanning transmission electron microscopy (STEM) and atom probe tomography (APT). **Figure 3** summarizes the characterization of the chemical composition and the structure at grain boundaries in both sample types. Figure 3a,b shows high angle angular dark field (HAADF) images and electron dispersive X-ray spectroscopy (EDS) elemental mappings of general grain boundaries in the nonequilibrium state (a) and after high temperature treatment (b).

The yttrium distribution at the interface is drastically changing from being homogeneous across the interface, to a strong segregation to the first B-site plane at the grain boundary. The differences are additionally highlighted by integrated line scans across the grain boundaries and along the [110] planes of the oriented grain on the right (Figure 2c,d). After high-temperature treatment, yttrium cations strongly segregate to the first B-site plane of the perovskite lattice and the grain boundary core, substituting large amounts of zirconium cations, thereby compensating the positive core charge.[29]

In addition to an elastic driving force induced by cationic size mismatch,[51,52] the segregation is driven by the space charge potential at the grain boundary, generated by oxygen vacancy accumulation.[26,28] This leads to high local yttrium

© 2024 The Author(s). Advanced Energy Materials published by Wiley-VCH GmbH

16146840, 2025, 9, Downloaded from https://advanced.onlinelibrary.wiley.com/doi/10.1002/aenm.202404410 by Forschungszentrum Jülich GmbH Research Center, Wiley Online Library on [07/03/2025]. See the Terms and Conditions (https://onlinelibrary.wiley.com/terms-and-conditions) on Wiley Online Library for rules of use; OA articles are governed by the applicable Creative Commons License

concentrations of ≈8 at% (estimated from EDS by a standard-less quantification) on the last B-site plane. This correlates to 43 at% of yttrium on the B-site, which is far above the solubility limit for yttrium in $BaZrO_3$-based perovskites.[53] The high local concentration of yttrium (which acts as a negative point defect, i.e., Y'_{Zr}) can partially compensate the positive core charge, decreasing the space charge potential and thereby lowering the barrier for proton conduction across the grain boundaries. This results in the strong increase in grain boundary conductivity (Figure 1f) and a decrease of the space charge potential (Figure 2a), measured using EIS.

Additionally, electron energy loss spectroscopy (EELS, Figure 2e,f) helps to understand the influence of segregation on the local oxygen bonding environment and the Ce valency at the grain boundary. Both graphs show integrated spectra of the same size (1 nm x 3 nm) taken from the grain boundary core and an adjacent "bulk" region (details on the EELS analysis can be found in Figure S2, Supporting Information). Nonequilibrium grain boundaries show a clear reduction in the intensity of the oxygen K edge and significant changes in the fine structure, induced by the depletion of oxygen in the grain boundary core.[54] However, the corresponding Ce $M_{4,5}$ edge does not reveal differences between bulk and grain boundary. After thermal annealing at 1600 °C clear changes in both the oxygen K and the Ce $M_{4,5}$ edge are visible (red spectra). Both intensity and fine structure of the oxygen K edge at the grain boundary are approaching the characteristics, which can be observed in the bulk. In contrast to the O K edge, the intensity of the Ce $M_{4,5}$ edge after thermal treatment decreases in intensity at the grain boundary, most likely due to a substitution of Ce^{4+} by Y^{3+} cations. Comparing the ratio of the intensities of the Ce M_5 to the M_4 edge, which can be used to assess the valence state of Ce,[6,55] did not reveal significant changes between bulk and grain boundary, before and after equilibration of the grain boundaries (0.74 to 0.73 for the SPS sample and 0.72 to 0.71 for the +1600 sample from bulk and GB measurements, respectively). Additionally, XPS measurements on bulk samples revealed no significant changes in the core-level signatures and in the relative composition of the sample in the nonequilibrium and equilibrium state, highlighting that changes in defect chemistry and electronic signature are truly localized to the grain boundary region, which is undetectable by XPS (details on the XPS analysis can be found in Figure S3, Supporting Information).

The gained insights on yttrium segregation from HR-STEM were also confirmed by electrostatic analysis and density functional theory (DFT) computing the segregation energy for Y and Yb cations that diffuse from bulk to GB lattice sites (details on the atomistic models and computational setup can be found in Figure S4, Supporting Information, and the method section). The segregation energies in a representative GB model simulating a symmetric Σ3 [110]/(-112) tilt GB for Y and Yb cations are calculated as −0.89 and −1.00 eV $atom^{-1}$, respectively. The segregation energies for Y and Yb are much larger than that calculated by A. Lindmann et al.[28] for Y without having oxygen vacancy at the GB (−0.32 eV). This is because the clustering of oxygen vacancies with Y^{3+}/Yb^{3+} cations is electrostatically more favorable than that with Zr^{4+}. This result shows that oxygen vacancies clearly increase the driving force for Y/Yb segregation at elevated temperatures.

As the chemical resolution of transmission electron microscopy techniques is insufficient to derive exact concentrations on the local defect chemistry, atom probe tomography (APT) was applied to assess the composition of grain boundaries after thermal annealing. Figure 3g–i shows the 3D reconstruction of an APT dataset, which includes five grain boundaries and a triple junction, as well as a concentration profile built across one of the grain boundaries. The high mass resolution and quantitative nature of APT allow for calculating of the Gibbsian interfacial excess $\Gamma_{i,}$ giving exact values for the segregation of yttrium and minor impurities (strontium and calcium) to the grain boundary (see Table S1, Supporting Information). An approximation of the Langmuir – McLean description for solute segregation, makes an estimation of the average diffusion coefficient D_Y of Y to the grain boundaries in BZCY possible using Equation (3),[56]

$$\frac{X_b(t) - X_b(0)}{X_b(\infty) - X_b(0)} = \frac{2}{\beta}\frac{b^2}{a^3}\left(\frac{4Dt}{\pi}\right)^{1/2} \tag{3}$$

where $X_b(t)$ is the concentration at the interface at different times, and a and b are the atomic sizes of the matrix and the solute atoms, respectively. And β is the ratio between the solute concentration at the grain boundary to the concentration at the bulk, $\beta = X_b/X_c$. More information about the calculation can be found in the method section.

For the segregation of yttrium from a completely nonequilibrated state to an average grain boundary excess of $\Gamma_Y = 6.3$ at/nm^2, a diffusion coefficient $D_Y = 0.25 \times 10^{-24}$ $m^2\ s^{-1}$ can be estimated. Compared to the bulk diffusion coefficients of cations in other perovskite oxides like $BaTiO_3$ and $SrTiO_3$, D_Y is comparably low,[57–59] which agrees well with the general refractive nature of this material, requiring high sintering temperatures (>1500 °C for BZCY compared to, e.g., 1150 °C for $BaTiO_3$). However, the driving force assumption for Equation (3) may not be complete as it ignores electrostatic contributions, and the presented value should be considered as an estimation. Note that this is a general issue of diffusion coefficients, particularly for grain boundary processes, and this study is one of the rare cases where an approximation is possible at all.

Furthermore, combining the high spatial resolution of STEM/EDS and the chemical resolution of APT enables us to calculate the atomic percentage of acceptor dopants on the last B-site plane at the grain boundary, giving an insight into the local chemistry. As the planar density of the B-site in Y-doped $BaZrO_3$ in the [100] plane is 6.25 at nm^{-2}, and the average yttrium excess at the grain boundary is 6.3 at nm^{-2} (distributed across both B-site planes at the GB and the GB core, see Figure 3d), all three atomic positions have an average 43.6 at% yttrium occupancy. Considering a bulk solubility of yttrium on the B-site of roughly 30 at%[60,61] the grain boundary composition we measured both in STEM-EDS and APT clearly surpasses these values and reveals a complexion-like thermodynamically stable grain boundary phase.[62]

However, the analysis of various GBs using APT also revealed deviations in interfacial acceptor dopant excess, varying between 4.9 and 7.9 at nm^{-2} (see Table S1, Supporting Information). This shows the strong influence the grain boundary character has on the segregation behavior, highlighting the need for further correlative microscopy and modelling approaches to reveal the

© 2024 The Author(s). Advanced Energy Materials published by Wiley-VCH GmbH

16146840, 2025, 9, Downloaded from https://advanced.onlinelibrary.wiley.com/doi/10.1002/aenm.202404410 by Forschungszentrum Jülich GmbH Research Center, Wiley Online Library on [07/03/2025]. See the Terms and Conditions (https://onlinelibrary.wiley.com/terms-and-conditions) on Wiley Online Library for rules of use; OA articles are governed by the applicable Creative Commons License

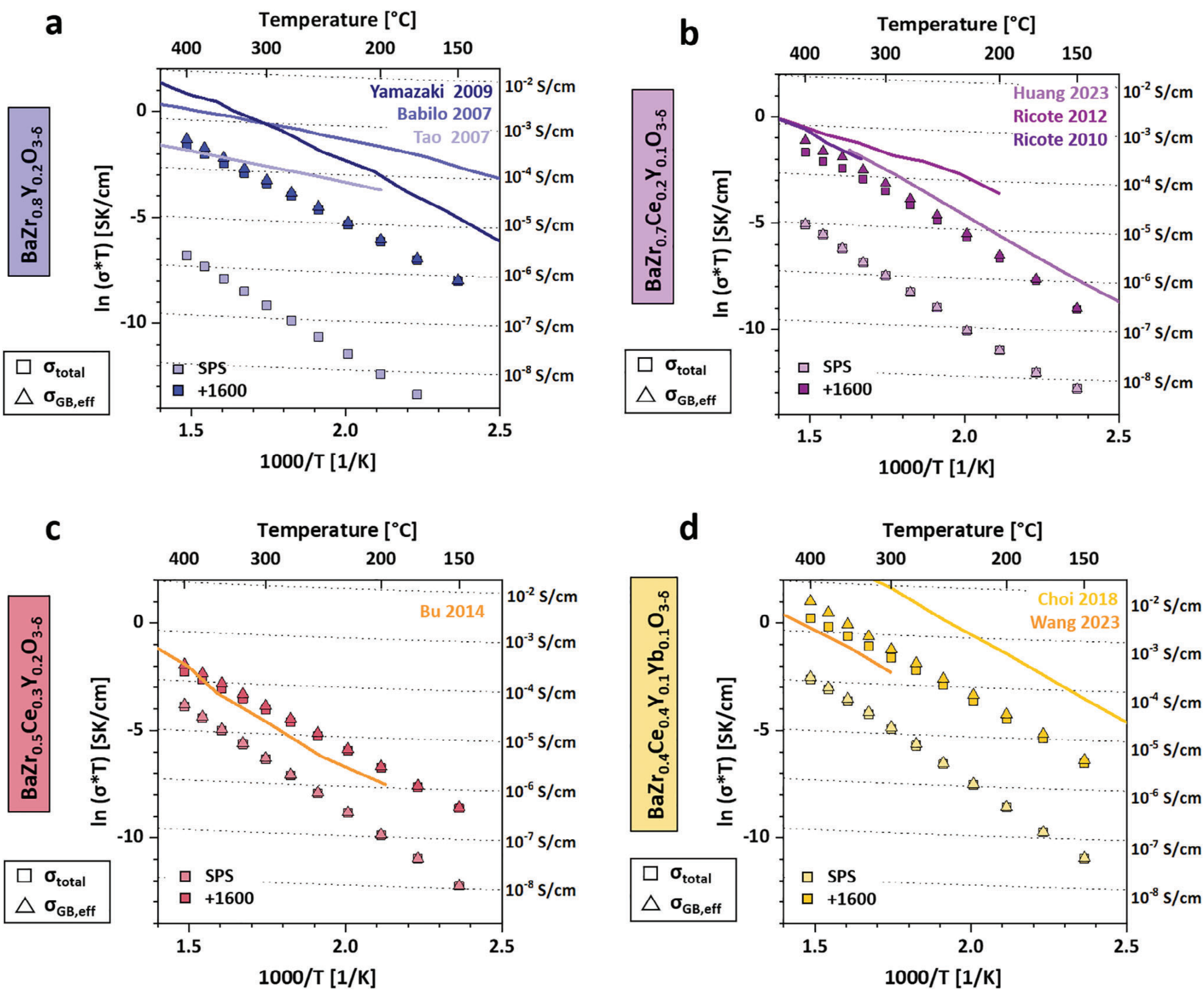

Figure 4. Segregation-controlled conductivity changes in different scientifically important $BaZrO_3$ based proton conductors. a–d) Electrochemical impedance spectroscopy in wet Ar/H_2 of $BaZr_{0.8}Y_{0.2}O_{3-\delta}$ (BZY20) (a), $BaZr_{0.7}Ce_{0.2}Y_{0.1}O_{3-\delta}$ (BZCY721) (b), $BaZr_{0.5}Ce_{0.3}Y_{0.2}O_{3-\delta}$ (BZCY532) (c), and $BaZr_{0.4}Ce_{0.4}Y_{0.1}Yb_{0.1}O_{3-\delta}$ (BZCYYB4411) (d) samples after SPS and post thermally treated for 5 h at 1600 °C in air. Total and effective grain boundary conductivity are represented by squares and triangles, respectively. Literature data in all plots is visualized by lines.[13,37,44,45,65–68]

fundamental relationships between segregation, grain boundary properties, and the related transport mechanisms.[63,64]

2.3. Segregation Controlled Conductivity in Other Relevant Proton Conducting Ceramics

Figure 4 compares the conductivity of the most important proton-conducting ceramics based on $BaZrO_3$. In addition to $BaZr_{0.7}Ce_{0.2}Y_{0.1}O_{3-\delta}$ (BZCY721, Figure 4b), we investigated compositions without cerium $BaZr_{0.8}Y_{0.2}O_{3-\delta}$ (BZY20, Figure 4a), with higher cerium contents $BaZr_{0.5}Ce_{0.3}Y_{0.2}O_{3-\delta}$ (BZCY532, Figure 4c) and a co-doped composition with high cerium content $BaZr_{0.4}Ce_{0.4}Y_{0.1}Yb_{0.1}O_{3-\delta}$ (BZCYYb4411, Figure 4d). All materials were sintered by FAST/SPS at low temperatures and short dwell times under mechanical pressure, to bring them into a densified and nonequilibrated state and afterward annealed for 5 h at 1600 °C. For both sample states, the total and the effective grain boundary conductivity are displayed, to showcase the impact a high-temperature equilibration of the grain boundary defect chemistry has on the performance of different ceramic proton conductors.

All compositions show a strong increase in total conductivity after the thermal treatment, mainly caused by the increase in effective grain boundary conductivity. The cerium content on the B-site of the perovskite has a positive effect on the performance in the nonequilibrated state, which is highest for compositions with a higher cerium content. The cerium-free composition (BZY20) shows the worst electrochemical performance in the nonequilibrium state, making it complicated to separate bulk and grain boundary contributions (details on the fitting of the electrochemical data can be found in Figure S5, Supporting Information), due

© 2024 The Author(s). Advanced Energy Materials published by Wiley-VCH GmbH

16146840, 2025, 9, Downloaded from https://onlinelibrary.wiley.com/doi/10.1002/aenm.202404410 by Forschungszentrum Jülich GmbH Research Center, Wiley Online Library on [07/03/2025]. See the Terms and Conditions (https://onlinelibrary.wiley.com/terms-and-conditions) on Wiley Online Library for rules of use; OA articles are governed by the applicable Creative Commons License

to the dominating impact of grain boundaries. Therefore, only the total conductivity can be derived from these measurements.

The increased diffusion coefficients for cations in $BaZrO_3$–$BaCeO_3$ solid solutions are leading to coarser microstructures (details on the microstructure can be found in Figure S6, Supporting Information) and might be one explanation for the continuous increase in conductivity in the nonequilibrated samples from BZY20 to BZCYYb4411. The higher interdiffusion clearly complicates the conservation of a nonequilibrium grain boundary defect chemistry during FAST/SPS.[59] Comparing our measurements to literature data, it becomes evident that the performance of conventionally processed protonic ceramics is reached after an equilibration of the grain boundary defect chemistry. Minor deviations can be observed only for several studies that used high temperature sintering (1600 °C) and extensive dwell times (24 h) to sinter BZY20[65,66] and BZCYYb4411.[13] These processing parameters exceed the thermal treatment applied here, leading to larger grain sizes and consequently a lower overall grain boundary resistance.

Our study reveals the fundamental importance of sufficiently high thermal treatments (either during sintering or by a post-thermal treatment) to enable acceptor dopant segregation to the grain boundary, compensating the positive core charge and lowering the intrinsic space charge potential. This behavior is responsible for the high protonic conductivity in all currently applied protonic ceramics, based on acceptor-doped $BaZrO_3$. Furthermore, the understanding of the relationship between thermal history and grain boundary defect chemistry can be a novel design parameter to optimize the properties of various electroceramics by tuning their grain boundary segregation.

3. Conclusion

In this study, we developed model materials based on the ceramic proton conductor $BaZr_{0.7}Ce_{0.2}Y_{0.1}O_{3-\delta}$, suitable for investigating the kinetics of solute segregation to grain boundaries and its influence on protonic conductivity. Through the systematic variation of thermal treatments between 1000 and 1600 °C, we were able to continuously increase the grain boundary conductivity by altering its defect chemistry from a nonequilibrium to an equilibrated state, without significant changes in the grain size. The drastic increase in protonic conductivity could be directly associated with the atomically sharp segregation of the yttrium acceptor dopant to the grain boundary after high-temperature treatment. The presence of negatively charged Y'_{Zr} point defects directly adjacent and in the grain boundary core compensates part of the intrinsic positive core charge, subsequently lowering the overall space charge potential and facilitating proton transport across grain boundaries.

The combination of high spatial resolution spectroscopy in STEM and the high 3D elemental sensitivity of APT allowed us to determine the local chemistry of nonequilibrium as well as equilibrated grain boundaries. This enabled us to derive the fundamental relationships between the measured protonic conductivity, the chemistry at grain boundaries, and the space charge potential while excluding the influence of sintering aids and varying microstructures. Our results highlight the importance of sufficiently high thermal treatments above 1300 °C, to facilitate acceptor dopant segregation and enable high protonic conductivities in this class of materials.

We could additionally show that this behavior can be observed in most commonly applied compositions of ceramic proton conductors based on $BaZrO_3$, independently of the B-site composition. Therefore, the fundamental insights reported here are applicable to a broad variety of materials used in solid oxide fuel and electrolysis cells, as well as membrane reactors. Even though the influence of acceptor dopant segregation has been exemplified for ceramic proton conductors here, the understanding of this behavior is highly relevant for a wide variety of functional ceramics, where control over grain boundary properties is essential in harnessing their optimal performance.

4. Experimental Section

Starting Powders and Sintering: In this study, commercial powders of the nominal composition $BaZr_{0.7}Ce_{0.2}Y_{0.1}O_{3-\delta}$ (BZCY721), $BaZr_{0.5}Ce_{0.3}Y_{0.2}O_{3-\delta}$ (BZCY532), and $BaZr_{0.4}Ce_{0.4}Y_{0.1}Yb_{0.1}O_{3-\delta}$ (BZCYYb4411, all Marion Technologies, France) as well as self-synthesized $BaZr_{0.8}Y_{0.2}O_{3-\delta}$ (BZY20) and $BaZr_{0.7}Ce_{0.2}Y_{0.1}O_{3-\delta}$ (0.5 wt% NiO, SSRS-BZCY721) powders have been applied. Details on the mixed oxide powder synthesis route can be found elsewhere.[35,47,69] All powders are sintered using a field assisted sintering / spark plasma sintering (FAST/SPS) device (HP-D5, FCT Systeme, Germany). Compositions with a low amount of Ce were densified at 1450 °C for 5 min with 80 MPa of uniaxial pressure applied, while Ce-rich compositions (BZCY532 and BZYYb4411) were sintered at 1350 °C for 5 min using a uniaxial pressure of 50 MPa. The heating and cooling rates for both experiments were 150 K min^{-1}, enabling fast densification and the preservation of a nonequilibrium grain boundary defect chemistry. All thermal treatments are done in air furnaces between 1000 and 1600 °C from 5 to 30 h. To prevent Ba evaporation at higher temperatures, thermal treatments above 1400 °C were conducted in sacrificial powder of the same composition.

Electrochemical Impedance Spectroscopy: Electrochemical impedance spectroscopy (EIS) was used to assess the proton conductivity of all samples investigated in the scope of this study. To separate bulk and grain boundary contributions, the impedance was measured in the range between 600 and 150 °C using an Alpha-A High Performance Frequency Analyzer, (Novocontrol, Germany) in the frequency range of 10 MHz to 0.1 Hz in wet Ar/2.9%H_2 ($p(H_2O) \approx 0.025$ bar). The impedance data was fitted using a series of equivalent circuits consisting of parallels of a resistance and constant phase element (R||CPE) and interpreted using the brick layer model[46] in RelaxIS3 (rhd instruments, Germany). The R||CPE elements were attributed to bulk, grain boundary, or electrode by calculating the specific capacitance.[46,70] Subsequently, the total, bulk and effective grain boundary conductivity are calculated using Equations (4–6), respectively. In the given equations R_b and R_{gb} are the resistivities derived from the fitting and l and A are the thickness and area of the measured sample.

$$\sigma_t = \frac{1}{(R_b + R_{gb})} \frac{l}{A} \tag{4}$$

$$\sigma_b = \frac{1}{R_b} \frac{l}{A} \tag{5}$$

$$\sigma_{eff.gb} = \frac{1}{R_{gb}} \frac{l}{A} \tag{6}$$

Scanning Transmission Electron Microscopy: Samples for scanning transmission electron microscopy (STEM) were prepared using a conventional dimpling route to achieve a large area of electron transparent materials, facilitating the search for suitable grain boundaries for high resolution analysis. Bulk samples were first metallographically ground and polished

© 2024 The Author(s). Advanced Energy Materials published by Wiley-VCH GmbH

16146840, 2025, 9, Downloaded from https://advanced.onlinelibrary.wiley.com/doi/10.1002/aenm.202404410 by Forschungszentrum Jülich GmbH Research Center, Wiley Online Library on [07/03/2025]. See the Terms and Conditions (https://onlinelibrary.wiley.com/terms-and-conditions) on Wiley Online Library for rules of use; OA articles are governed by the applicable Creative Commons License

to a thickness of 100 µm and afterward dimple grinded to a minimal thickness of 10–15 µm using a dimple grinder (Gatan Inc., USA). Afterward, the final hole was milled and thinned using an Ar ion milling device (PIPS II, Gatan Inc., USA). High resolution STEM imaging and spectroscopy was done using a probe C_s-corrected Spectra 300 microscope (Thermo Fischer Scientific, USA) at 200 keV. The microscope is equipped with a Super-X EDS detector and a Gatan Continuum 1066 energy filter (GIF). Data analysis of the EDS results was done using the Velox software (Thermo Fischer Scientific, USA). Quantification of the EDS measurements was done using a standard less (Cliff-Lorimer) method to estimate the composition at the grain boundary. High errors are assumed as the quantification does not consider absorption and channeling. The analysis of the EELS data was done using the Python package HyperSpy.

Atom Probe Tomography: APT specimens were prepared from the polished sample surface by the conventional lift-out technique using a dual-beam focused-ion-beam (FIB) system (FEI Helios Nanolab 600i). To reduce Ga implantation in the APT-ready sample, 2 keV Ga beam was used for final cleaning of specimens. APT analyses were performed using a reflectron-equipped local electrode atom probe tool (LEAP 4000X HR, Cameca Instruments, USA) in laser mode. Laser pulses of 355 nm wavelength, 12 ps pulse length, 10–20 pJ pulse energy, and 200 kHz frequency were applied. The specimen base temperature was kept at ≈25 K and the detection rate was maintained at 0.005 or 0.01 ion per pulse. Data reconstruction and analysis was performed using Cameca IVAS 3.6.14 software package. Reconstruction parameters were derived from comparing the pre- and post-analysis SEM images of APT specimens, so that correct dimensions of the reconstructed dataset (final specimen radius and the length of the field-evaporated volume) are ensured. Three APT datasets, each containing 2–5 grain boundaries, were analyzed in total.

Density Functional Theory Calculations: Grain boundary (GB) models were constructed by using Aimsgb[71] employing 48 formula units of BZO, containing two identical grain boundaries, due to periodic boundary conditions. First, the most favorable sites for two oxygen vacancies and four Y/Yb ions in a GB $\Sigma 3[110]/(-112)$ grain boundary (GB) by performing Coulomb energy calculations on 2 003 395 680 (2.0 × 109) possible combinations/permutations employing the Supercell code were found.[72] Charges of 2+ for Ba, 4+ for Zr, 3+ for Y/Yb, and 2- for oxygen were used. To model the SPS-sintered GB, a similar approach was utilized. To accommodate Y/Yb ions in the bulk region of our GB model, two fixed trivalent ions next to the optimal oxygen vacancy position at the GB to repel four Y/Yb ions from the GB plane were artificially introduced. To maintain the charge neutrality for this case, the Zr valence was reduced to +3.952 in this step. Subsequently, the artificially added trivalent ions at the GB plane were replaced by Zr ions. The resulting models are depicted in Figure S4 (Supporting Information). To calculate the segregation energy, which is the total energy difference between Y/Yb at the GB plane and bulk region ($E_{Y/Yb}(GB)-E_{Y/Yb}(Bulk)$), spin-polarized DFT[73,74] calculations as implemented in the Vienna Ab initio Simulation Package (VASP) code[75] using the PBE functional[76] and the Projector Augmented-Wave (PAW) method were performed.[77] A Γ-point centered k-point mesh of 2 × 1 × 4 and energy cut-off of 520 eV as well as energy and force convergence criteria of 5.0×10^{-5} eV and 1.0×10^{-2} eV Å^{-1}, respectively, were applied. Ionic positions and unit cell volume were fully optimized while the unit cell shape was fixed (ISIF = 8). Pseudopotentials with valence electron configurations 5s2 $5p^6$ $5d^{0.01}$ $6s^{1.99}$, 2s2 $2p^4$, 4s2 $4p^6$ 4d3 $5s^1$, 4s2 $4p^6$ 4d2 $5s^1$, $5p^6$ $5d^1$ 6s2 for Ba, O, Zr, Y, and Yb were used, respectively.

Calculation of Space Charge Potential and Y Diffusion Coefficients: Space charge potentials were evaluated using Equation (2) which is the solution of an 1D Poisson equation of a Schottky depletion layer.[48] In Equation (2), R is the Boltzmann constant, F the Faraday constant, Φ_0 the space charge potential, z_j the valency of the mobile charge carrier (z_j = 1 for Protons), e the elementary charge, T the temperature in K during EIS and, ω_{Bulk} and ω_{GB} are the relaxation frequencies of the bulk's and GBs' impedance signal. Either the ratio of the bulk's and grain boundaries' resistivity, capacitance, relaxation frequency or relaxation times can be used for space charge potential calculations. Either of these parameters are obtained from fitting impedance data with the aforementioned equivalent circuit. Relaxation frequencies were calculated using Equation (7), where R_i and C_i are the total resistance and capacitance of the bulk or GB. Using the relaxation times or frequency give the best agreement with the true space charge potential at the GBs because these parameters are microstructure independent.[78]

$$\omega_i = \frac{1}{2\pi \cdot R_i C_i} \tag{7}$$

The diffusion coefficient for Yttrium segregation to grain boundaries was estimated using a Langmuir–McLean-based model, where the segregation kinetics can be described by Equation (8),[56]

$$\frac{X_b\,(t) - X_b\,(0)}{X_b\,(\infty) - X_b\,(0)} = 1 - \exp\left(\frac{4Dt}{\beta^2 f^2}\right) erfc \left(\frac{4Dt}{\beta^2 f^2}\right)^{1/2} \tag{8}$$

where $X_b(t)$ is the concentration at the interface at different times, f is a ratio between the atomic sizes $f = a^3 b^{-2}$ with a for the matrix and b for the solute. And β is the ratio between the concentration at the grain boundary to the concentration at the bulk, $\beta = X_b/X_c$.

For short dwell times below a full equilibration, this equation can be approximated by:[56]

$$\frac{X_b\,(t) - X_b\,(0)}{X_b\,(\infty) - X_b\,(0)} = \frac{2}{\beta}\,\frac{b^2}{a^3}\left(\frac{4Dt}{\pi}\right)^{1/2} \tag{9}$$

In the above applied estimation, we used the cationic size ratios of Y and Zr/Ce for b and a, as well as the atomic concentrations of Y on the B-site from APT measurements ($X_b(t)$ = 44.3 at% and $X_b(0)$ = 20.0 at%). The thermodynamic maximum of segregation was estimated to be 50 at%.

Photoelectron X-Ray Spectroscopy: XPS (Phi 5000 VersaProbe, ULVAC Phi, Physical Electronics Inc.) was performed for the nonequilibrium and equilibrium sample state using the Al Kα1 line (E_λ = 1486.6 eV) of a monochromized X-ray source. Survey spectra and O 1s, C 1s, Si 2p, Ce 3d, Ba 3d, Zr 3d, Y 3d core-level spectra were obtained at a photoemission angle of $\theta = 15°$. Survey measurements were performed using a pass energy of E_0 = 187.85 eV. For the analysis of core-level spectra, the pass energy was kept constant at E_0 = 23.5 eV for high energy resolution in the fixed analyzer transmission mode.

All spectra were aligned with respect to the C 1s core-level signal BE = 284.8 eV. The survey spectra were normalized to the background signal between ΔBE = 60–70 eV. Core-level spectra were normalized to the pre-peak region (ΔBE(O 1s) = 520–524 eV, ΔBE(Ce 3d) = 873–876 eV, ΔBE(Ba 3d) = 770–774 eV, ΔBE(Zr 3d) = 172–174 eV, ΔBE(Y 3d) = 147–149 eV). No background subtraction is applied. An offset is used along the y-axis to display the spectra to improve clarity. KolXPD version 1.8.0 was used for the evaluation of the data.

Supporting Information

Supporting Information is available from the Wiley Online Library or from the author.

Acknowledgements

Dr. Egbert Wessel (IMD-1, Forschungszentrum Jülich GmbH) is acknowledged for EBSD measurements. M.K is acknowledging the financial support from the DFG in the project MA 1280/69-1 and GU 993/14-1. J.E., D.J., M.P.Z. and W.R. thank the DFG for funding within the Emmy Noether program (RH 146/1-1). J.M.S., S.E. and L.A. are acknowledging financial support by the Spanish Ministry of Science and Innovation (PID2022-139663OB-100 and CEX2021-001230-S grants funded by MCIN/AEI/10.13039/501100011033). P.K. and S.K. are acknowledging computing time granted through JARA-HPC on the supercomputer JURECA at Forschungszentrum Jülich under grant No. jiek12 and funding from the European Union under grant agreement No. 101099717 – ECOLEFINS project.

Open access funding enabled and organized by Projekt DEAL.

© 2024 The Author(s). Advanced Energy Materials published by Wiley-VCH GmbH

16146840, 2025, 9, Downloaded from https://advanced.onlinelibrary.wiley.com/doi/10.1002/aenm.202404410 by Forschungszentrum Jülich GmbH Research Center, Wiley Online Library on [07/03/2025]. See the Terms and Conditions (https://onlinelibrary.wiley.com/terms-and-conditions) on Wiley Online Library for rules of use; OA articles are governed by the applicable Creative Commons License

Conflict of Interest

The authors declare no conflict of interest.

Data Availability Statement

The data that support the findings of this study are available from the corresponding authors upon reasonable request.

Keywords

defect segregation, grain boundaries, protonic ceramics, space charge

Received: September 24, 2024
Revised: November 28, 2024
Published online: December 23, 2024

[1] J. F. Nie, Y. M. Zhu, J. Z. Liu, X. Y. Fang, *Science* **2013**, *340*, 957.
[2] J. P. Buban, K. Matsunaga, J. Chen, N. Shibata, W. Y. Ching, T. Yamamoto, Y. Ikuhara, *Science* **2006**, *311*, 212.
[3] H. Zhao, Y. Yin, Y. Wu, S. Zhang, A. M. Mingers, D. Ponge, B. Gault, M. Rohwerder, D. Raabe, *Nat. Commun.* **2024**, *15*, 1.
[4] W. Lee, H. J. Jung, M. H. Lee, Y.-B. Kim, J. S. Park, R. Sinclair, F. B. Prinz, *Adv. Funct. Mater.* **2012**, *22*, 965.
[5] X. Guo, R. Waser, *Prog. Mater. Sci.* **2006**, *51*, 151.
[6] W. J. Bowman, J. Zhu, R. Sharma, P. A. Crozier, *Solid State Ionics* **2015**, *272*, 9.
[7] H. J. Avila-Paredes, S. Kim, *Solid State Ionics* **2006**, *177*, 3075.
[8] J. Janek, W. G. Zeier, *Nat. Energy* **2016**, *1*, 1.
[9] T. Schmaltz, F. Hartmann, T. Wicke, L. Weymann, C. Neef, J. Janek, *Adv. Energy Mater.* **2023**, *13*, 2301886.
[10] L. Yang, S. Wang, K. Blinn, M. Liu, Z. Liu, Z. Cheng, M. Liu, *Science* **2009**, *326*, 126.
[11] E. Vøllestad, R. Strandbakke, M. Tarach, D. Catalán-Martínez, M.-L. Fontaine, D. Beeaff, D. R. Clark, J. M. Serra, T. Norby, *Nat. Mater.* **2019**, *18*, 752.
[12] C. Duan, R. J. Kee, H. Zhu, C. Karakaya, Y. Chen, S. Ricote, A. Jarry, E. J. Crumlin, D. Hook, R. Braun, N. P. Sullivan, R. O'Hayre, *Nature* **2018**, *557*, 217.
[13] S. Choi, C. J. Kucharczyk, Y. Liang, X. Zhang, I. Takeuchi, H.-I. Ji, S. M. Haile, *Nat. Energy* **2018**, *3*, 202.
[14] A. Hauch, R. Küngas, P. Blennow, A. B. Hansen, J. B. Hansen, B. V. Mathiesen, M. B. Mogensen, *Science* **2020**, *370*, aba6118.
[15] W. Deibert, M. E. Ivanova, S. Baumann, O. Guillon, W. A. Meulenberg, *J. Memb. Sci.* **2017**, *543*, 79.
[16] V. Kyriakou, I. Garagounis, A. Vourros, E. Vasileiou, A. Manerbino, W. G. Coors, M. Stoukides, *Appl. Catal. B Environ.* **2016**, *186*, 1.
[17] H. Malerød-Fjeld, D. Clark, I. Yuste-Tirados, R. Zanón, D. Catalán-Martinez, D. Beeaff, S. H. Morejudo, P. K. Vestre, T. Norby, R. Haugsrud, J. M. Serra, C. Kjølseth, *Nat. Energy* **2017**, *2*, 923.
[18] C. Clark, H. Malerod-fjeld, M. Budd, I. Yuste-Tirados, D. Beeaff, S. Aamodt, K. Nguyen, L. Ansaloni, T. Peters, P. K. Vestre, D. K. Pappas, M. I. Valls, S. Remiro-Buenamana, T. Norby, T. S. Biorheim, J. M. Serra, C. Kjolseth, *Science* **2022**, *376*, 390.
[19] D. Ding, Y. Zhang, W. Wu, D. Chen, M. Liu, T. He, *Energy Environ. Sci.* **2018**, *11*, 1710.
[20] J. M. Serra, *Nat. Energy* **2019**, *4*, 178.
[21] C. Duan, J. Huang, N. Sullivan, R. O'Hayre, *Appl. Phys. Rev.* **2020**, *7*, 011314.
[22] K. D. Kreuer, *Annu. Rev. Mater. Res.* **2003**, *33*, 333.
[23] K. H. Ryu, S. M. Haile, *Solid State Ionics* **1999**, *125*, 355.
[24] K. Katahira, Y. Kohchi, T. Shimura, H. Iwahara, *Solid State Ionics* **2000**, *138*, 91.
[25] R. A. De Souza, *Phys. Chem. Chem. Phys.* **2009**, *11*, 9939.
[26] R. A. De Souza, Z. A. Munir, S. Kim, M. Martin, *Solid State Ionics* **2011**, *196*, 1.
[27] E. E. Helgee, A. Lindman, G. Wahnström, *Fuel Cells* **2013**, *13*, 19.
[28] A. Lindman, T. S. Bjørheim, G. Wahnström, *J. Mater. Chem. A* **2017**, *5*, 13421.
[29] M. Shirpour, B. Rahmati, W. Sigle, P. A. van Aken, R. Merkle, J. Maier, *J. Phys. Chem. C* **2012**, *116*, 2453.
[30] M. Shirpour, R. Merkle, J. Maier, *Solid State Ionics* **2012**, *216*, 1.
[31] M. Shirpour, R. Merkle, C. T. Lin, J. Maier, *Phys. Chem. Chem. Phys.* **2012**, *14*, 730.
[32] M. Shirpour, G. Gregori, L. Houben, R. Merkle, J. Maier, *Solid State Ionics* **2014**, *262*, 860.
[33] D. R. Clark, H. Zhu, D. R. Diercks, S. Ricote, R. J. Kee, A. Almansoori, B. P. Gorman, R. P. O'Hayre, *Nano Lett.* **2016**, *16*, 6924.
[34] M. Shirpour, R. Merkle, J. Maier, *Solid State Ionics* **2012**, *225*, 304.
[35] M. Kindelmann, J. N. Ebert, D. Jennings, D. Sebold, W. Rheinheimer, M. Bram, J. Mayer, O. Guillon, *J. Eur. Ceram. Soc.* **2023**, *44*, 2744.
[36] C. Kjølseth, H. Fjeld, Ø. Prytz, P. I. Dahl, C. Estournès, R. Haugsrud, T. Norby, *Solid State Ionics* **2010**, *181*, 268.
[37] Y. Huang, R. Merkle, D. Zhou, W. Sigle, P. A. van Aken, J. Maier, *Solid State Ionics* **2023**, *390*, 116113.
[38] D. R. Clark, D. R. Diercks, S. Ricote, T. Tauer Dearden, N. P. Sullivan, J. W. Medlin, B. P. Gorman, R. P. O'Hayre, *J. Mater. Chem. C* **2023**, *11*, 5082.
[39] M. Kindelmann, S. Escolastico, L. Almar, A. Vayyala, D. Jennings, W. Deibert, W. A. Meulenberg, W. Rheinheimer, M. Bram, J. M. Serra, J. Mayer, O. Guillon, *J. Mater. Chem. A* **2024**, *12*, 3977.
[40] A. L. Usler, R. A. De Souza, *J. Electrochem. Soc.* **2021**, *168*, 056504.
[41] A. L. Usler, F. Ketter, R. A. De Souza, *Phys. Chem. Chem. Phys.* **2024**, *26*, 8287.
[42] M. P. Zahler, D. Jennings, M. Kindelmann, O. Guillon, W. Rheinheimer, *J. Eur. Ceram. Soc.* **2023**, *43*, 6925.
[43] J. Wallis, S. Ricote, K. D. Weltmann, E. Burkel, A. Kruth, *Ceram. Int.* **2021**, *47*, 15349.
[44] S. Ricote, N. Bonanos, *Solid State Ionics* **2010**, *181*, 694.
[45] S. Ricote, N. Bonanos, A. Manerbino, W. G. Coors, *Int. J. Hydrogen Energy* **2012**, *37*, 7954.
[46] J. T. S. Irvine, D. C. Sinclair, A. R. West, *Adv. Mater.* **1990**, *2*, 132.
[47] J. N. Ebert, D. Jennings, L.-A. Schäfer, D. Sebold, W. Rheinheimer, *Scr. Mater.* **2024**, *241*, 0.
[48] J. Fleig, S. Rodewald, J. Maier, *J. Appl. Phys.* **2000**, *87*, 2372.
[49] G. Gregori, R. Merkle, J. Maier, *Prog. Mater. Sci.* **2017**, *89*, 252.
[50] F. Iguchi, N. Sata, H. Yugami, *J. Mater. Chem.* **2010**, *20*, 6265.
[51] M. Kindelmann, K. Ran, W. Rheinheimer, K. Morita, J. Mayer, M. Bram, O. Guillon, *J. Am. Ceram. Soc.* **2021**, *104*, 4946.
[52] D. Kim, R. Bliem, F. Hess, J.-J. Gallet, B. Yildiz, *J. Am. Chem. Soc.* **2020**, *142*, 3548.
[53] Y. Yamazaki, P. Babilo, S. M. Haile, *Chem. Mater.* **2008**, *20*, 6352.
[54] D. Jennings, J. N. Ebert, H. Du, Q. Ma, L.-A. Schäfer, D. Sebold, J. Mayer, W. Rheinheimer, *Chem. Mater.* **2023**, *35*, 8382.
[55] H. Hojo, T. Mizoguchi, H. Ohta, S. D. Findlay, N. Shibata, T. Yamamoto, Y. Ikuhara, *Nano Lett.* **2010**, *10*, 4668.
[56] M. P. Seah, *J. Phys. F Met. Phys.* **1980**, *10*, 1043.
[57] K. Gömann, G. Borchardt, M. Schulz, A. Gömann, W. Maus-Friedrichs, B. Lesage, O. Kaïtasov, S. Hoffmann-Eifert, T. Schneller, *Phys. Chem. Chem. Phys.* **2005**, *7*, 2053.
[58] S. Koerfer, R. A. De Souza, H. I. Yoo, M. Martin, *Solid State Sci.* **2008**, *10*, 725.

© 2024 The Author(s). Advanced Energy Materials published by Wiley-VCH GmbH

16146840, 2025, 9, Downloaded from https://advanced.onlinelibrary.wiley.com/doi/10.1002/aenm.202404410 by Forschungszentrum Jülich GmbH Research Center, Wiley Online Library on [07/03/2025]. See the Terms and Conditions (https://onlinelibrary.wiley.com/terms-and-conditions) on Wiley Online Library for rules of use; OA articles are governed by the applicable Creative Commons License

[59] I. Hasle, S. P. Waldow, U. N. Gries, R. A. De Souza, E. Vøllestad, R. Haugsrud, *J. Mater. Chem. A* **2021**, *9*, 21142.
[60] E. Fabbri, D. Pergolesi, S. Licoccia, E. Traversa, *Solid State Ionics* **2010**, *181*, 1043.
[61] M. D. Gonçalves, P. S. Maram, R. Muccillo, A. Navrotsky, *J. Mater. Chem. A* **2014**, *2*, 17840.
[62] P. R. Cantwell, M. Tang, S. J. Dillon, J. Luo, G. S. Rohrer, M. P. Harmer, *Acta Mater.* **2014**, *62*, 1.
[63] W. J. Bowman, A. Darbal, P. A. Crozier, *ACS Appl. Mater. Interfaces* **2020**, *12*, 507.
[64] H. Vahidi, A. Mejia, S. Xuan, A. Cassiadoro, A. Abdi, D. Mebane, W. Bowman, *ChemAxiv* **2024**.
[65] P. Babilo, T. Uda, S. M. Haile, *J. Mater. Res.* **2007**, *22*, 1322.
[66] Y. Yamazaki, R. Hernandez-Sanchez, S. M. Haile, *Chem. Mater.* **2009**, *21*, 2755.
[67] J. Bu, P. G. Jönsson, Z. Zhao, *J. Power Sources* **2014**, *272*, 786.
[68] M. Wang, W. Wu, Y. Lin, W. Tang, G. Gao, H. Li, F. F. Stewart, L. Wang, Y. Yang, D. Ding, *ACS Appl. Energy Mater.* **2023**, *6*, 8316.
[69] W. Deibert, M. E. Ivanova, Y. Huang, R. Merkle, J. Maier, W. A. Meulenberg, *J. Mater. Chem. A* **2021**, *3*.
[70] J. G. Lyagaeva, G. K. Vdovin, D. A. Medvedev, *J. Phys. Chem. C* **2019**, *123*, 21993.
[71] J. Cheng, J. Luo, K. Yang, *Comput. Mater. Sci.* **2018**, *155*, 92.
[72] K. Okhotnikov, T. Charpentier, S. Cadars, *J. Cheminform.* **2016**, *8*, 17.
[73] P. Hohenberg, W. Kohn, *Phys. Rev.* **1964**, *136*, B864.
[74] W. Kohn, L. J. Sham, *Phys. Rev.* **1965**, *140*, A1133.
[75] G. Kresse, J. Furthmüller, *Phys. Rev. B* **1996**, *54*, 11169.
[76] J. P. Perdew, K. Burke, M. Ernzerhof, *Phys. Rev. Lett.* **1996**, *77*, 3865.
[77] P. E. Blöchl, *Phys. Rev. B* **1994**, *50*, 17953.
[78] J. Fleig, *Solid State Ionics* **2002**, *150*, 181.

© 2024 The Author(s). Advanced Energy Materials published by Wiley-VCH GmbH

16146840, 2025, 9, Downloaded from https://advanced.onlinelibrary.wiley.com/doi/10.1002/aenm.202404410 by Forschungszentrum Jülich GmbH Research Center, Wiley Online Library on [07/03/2025]. See the Terms and Conditions (https://onlinelibrary.wiley.com/terms-and-conditions) on Wiley Online Library for rules of use; OA articles are governed by the applicable Creative Commons License